Microsyst Technol (2017) 23:5571–5585
DOI 10.1007/s00542-017-3361-5

TECHNICAL PAPER

Modelling and characterization of a robust, low-power and wide-range thermal wind sensor

Yanqing Zhu[1] · Ming Qin[1] · Yizhou Ye[1] · Zhenxiang Yi[1] · Kewen Long[2] · Qing-an Huang[1]

Received: 13 January 2017 / Accepted: 7 March 2017 / Published online: 14 March 2017

Abstract In this paper, we present a robust, low-power and wide-range MEMS thermal wind sensor, which is based on a glass reflow process. A general analytical model is first proposed for obtaining the heater's temperature and the temperature distribution on the sensor surface. Based on this model, the effect of the sensor's geometry and package on the sensor's performance is investigated. These results demonstrate how the measurement range and the sensitivity of the sensor can be optimized with a change in structural geometries. Besides, it has shown that the package structure of the sensor is also important for obtaining the required performance. Then, calculated results are validated with 2-D finite element method (FEM) solver CMOSOL. It is found that although there is some deviation between theoretical and simulation results, the model can have good reference value for latter MEMS thermal wind sensor design. Finally, the sensor is characterized in a wind tunnel. At a constant heating power of 14.5 mW, measurement results show that the sensor can detect airflow speeds of up to 33 m/s, with an accuracy better than 0.5 m/s at low speeds and 5% Full-Scale at high speeds. Airflow direction can be determined in a 360° range with an accuracy better than 5°. In addition, the sensor also shows a good repeatability.

✉ Ming Qin
mqin@seu.edu.cn

[1] Key Laboratory of MEMS of Ministry of Education, Southeast University, Nanjing 210096, China

[2] Foshan Chuandong Magnetic Electronics Co., Ltd, Foshan 528513, China

1 Introduction

The accurate measurements of wind speed and direction are essential to various aspects of daily life and industrial production (Connell 1982; Aylor 1990; Zhao et al. 2004; Arritt et al. 2007; Kumar et al. 2008). Therefore, wind sensors are widely used in different fields such as agricultural production, transportation, energy acquisition and equipment manufacturing, etc. In recent years, with the development of microelectromechanical systems (MEMS) technology, a variety of new MEMS wind sensors are emerging (Nguyen 1997). Among them, MEMS thermal wind sensors have drawn a great attention because of their advantages of non movable structure, high initial sensitivity, small volume and low cost (Zhu et al. 2014). However, thermal wind sensors also have a main drawback. They consume much more power than their counterparts such as mechanical and ultrasonic anemometers because the sensor chips need to be heated to above ambient temperature. This limits their application in embedded autonomous wireless sensor networks, mobile meteorological measuring equipments and other low-power occasions. To address this issue, numerous power-dissipation decrement approaches have been developed, categorized as using anisotropic wet etching of sensor substrate from either front-side or backside (Baltes et al. 1998; Kim et al. 2003; Sabaté et al. 2004; Adamec and Thiel 2010; Cubukcu et al. 2010), using low thermal conductivity substrates (Kaltsas et al. 2002; Shen et al. 2010; Vilares et al. 2010) and elevating the thermal elements away from the surface of the sensor substrates (Ebefors et al. 1998; Chen and Liu 2003; Sadeghi et al. 2013; Liu et al. 2015). Although these methods effectively reduce the power consumption of thermal wind sensors, there are also a series of drawbacks, including the need of protecting the sensor structures (i.e., hot-wires, cantilevers

and thin membranes) from the thermal stress caused by temperature changes, the contamination from dust and moisture in the air or being destroyed by the vibration and mechanical shocks (Li and Jiang 2008). Besides, the wire bonding wires used in the electrical connection between MEMS chips and the external circuit are usually exposed to the environment directly, which is not reliable for some applications in high temperature or high humidity conditions (Harman 1993).

To obtain a robust and low power thermal wind sensor that can be applied in practice, a glass-in-silicon reflow process has been introduced to fabricate the device (Zhu et al. 2016). The sensor takes a low thermal conductivity glass substrate to minimize the invalid heat loss and employs vertical silicon through-wafer interconnects to replace the bonding wires on the front surface of the chip. Besides, a passivation layer of nitride is deposited on the surface of the wind sensor to prevent direct exposure of the sensing elements to harsh media. The measurement results show that the sensor can be operated with a heating power as low as 4.8 mW. However, the drawbacks of this wind sensor is that it can only detect airflow speeds of up to 17.5 m/s, which is not satisfactory for many application situations. Thus, in this work, we present a measurement range enlarged thermal wind sensor which is based on the calorimetric principle. The sensor contains four orthogonally placed heaters and nine thermistors. Eight thermistors measure the temperature differences between the upstream and downstream surface of the sensor while one thermistor is positioned at the center to sense the average temperature of the chip. Because of using the same reflow process, the sensor also features of low power consumption and high reliability. On top of that, the thermal wind sensor and its package is analytically modeled, which is important for the sensor design and has not been done in previous works. The whole work is organized as follows: In Sect. 2 the sensor structure design and its package are presented. Moreover, the fabrication process and results of thermal wind sensors are discussed; Sect. 3 first gives the analytical model of the sensor, and then presents the design criterion of the sensor in accordance with the model. At last the validity of the model is verified by FEM simulations made with COMSOL Multiphysics software; Sect. 4 discusses in detail the experiment results of the DC characterization and output characteristics of the wind sensor; Sect. 5 finally summarizes the paper in a conclusion.

2 Sensor description

Figure 1 shows the schematic of the cross-section view of the proposed 2D thermal wind sensor. The wind sensor mainly consists of four parts, including a glass substrate

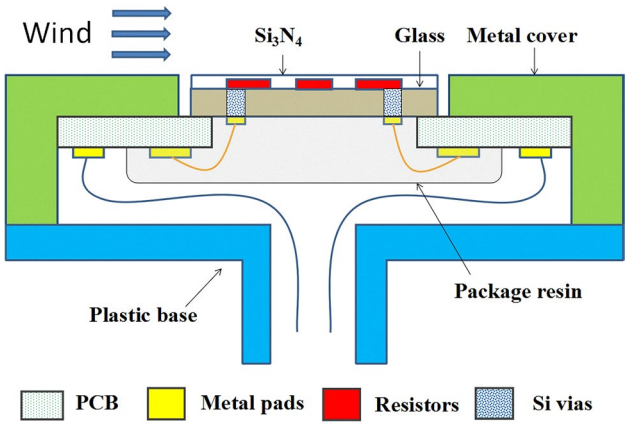

Fig. 1 Schematic cross-section view of the packaged thermal wind sensor

with embedded vertical silicon vias, metal pads, Si_3N_4 passivation layer, and metal resistors for heating and sensing temperature. When the sensor is operated, the heater heated the chip to above the ambient temperature. At zero flow velocity, the temperature profile around the heaters is symmetric, but forced convection will transport the heat downstream when a fluid passes over the heater. As a result, the temperature profile around the heaters will be asymmetric. The sensing resistors up- and downstream the heater will read different temperatures, and this temperature difference among the sensing elements can be used to determine the magnitude and direction of the wind. Because the passivation layer is extremely thin and the thermal conductivity of the glass substrate is very low, the thermal interaction between the proposed sensor and the airflow can be achieved effectively, and the unwanted heat loss from the heater to the surroundings is decreased. In this manner, the sensor can be operated with very low power dissipation and has a high sensitivity. Besides, the proposed sensor employs vertical silicon through-wafer interconnects to replace the bonding wires on the front surface of the chip, which enables the MEMS thermal wind sensor have more reliable electrical connections. Figure 1 also shows the package conditions of the proposed thermal wind sensor. As shown in the figure, the sensor was placed on the central opening of a PCB board with face upward, and wire bonded to the PCB board through the metal pads on the back side. In order to achieve good environmental isolation, the bonding wires were encapsulated by the packaging resin of poor thermal conductivity. Furthermore, a metal cover with a square hole in the middle was placed on the wind sensing side of the chip to obtain a smooth flowing surface and a plastic base provided the mechanical support for the sensor.

The proposed wind sensors could be fabricated with a glass reflow process (Zhu et al. 2016), as shown in Fig. 2. The main process flow can be divided into several steps: (a)

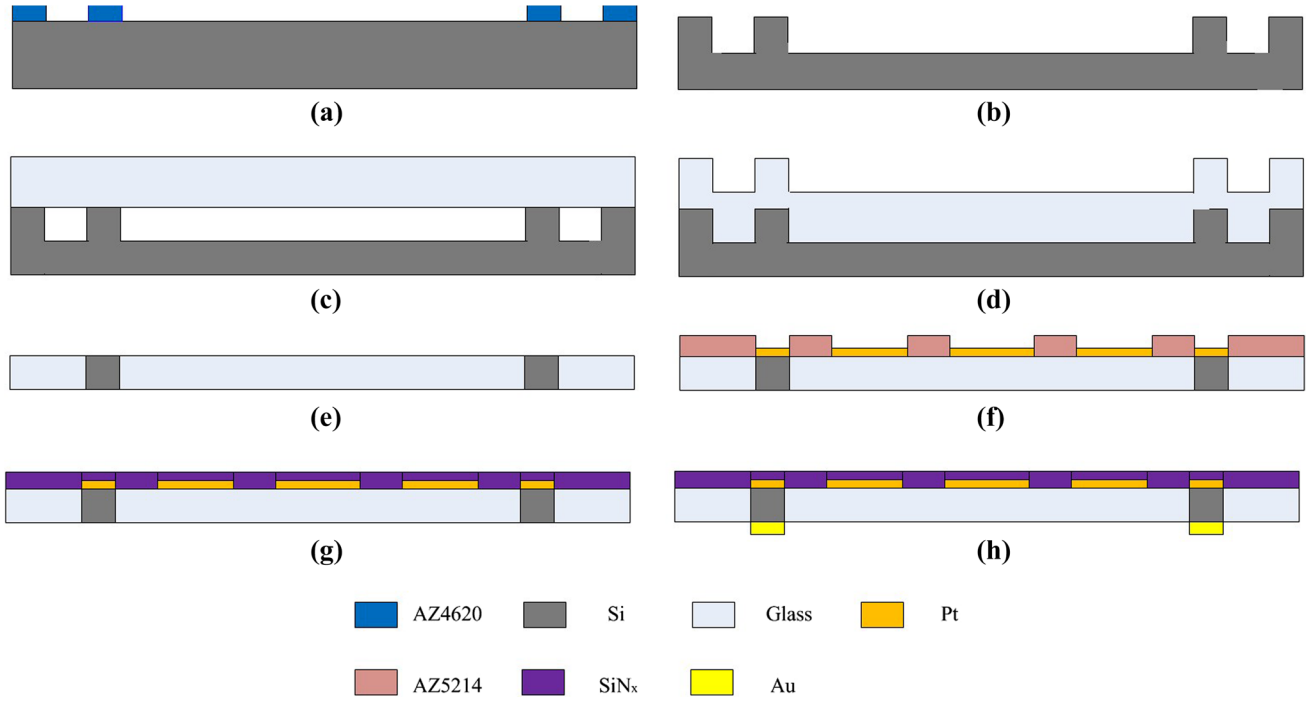

Fig. 2 Fabrication process of the proposed thermal wind sensor

the area of silicon vias for electrical conduction were firstly defined on the wafer surface using 10 μm thick AZ4620 photoresist in photolithography. (b) Then deep reactive ion etching (DRIE) process was then carried out to etch the silicon to obtain the cavities with a depth of 250 μm. (c) After that, a Borosilicate glass wafer of 500 μm thickness was anodically bonded to the etched silicon wafer at 400 °C and high vacuum level (about 5 mTorr). Before anodic bonding, the wafers need to be cleaned in oxygen plasma for 15 min. (d) The bonded glass was then reflowed in a furnace at 950 °C for 2 h. (e) Finally, the wafer was lapped to be 180–190 μm thick so that the through-wafer silicon vias would be exposed entirely. (f) 200 nm thick Pt was sputtered and patterned on the substrate by the lift-off process for the heaters and sensing elements of the sensor. 20 nm thick Ti was sputtered on the substrate before Pt to enhance the adhesion between the Pt layer and the substrate. (g) A low-stress 3000 Å-thick Si_3N_4 film was deposited utilizing a low temperature Plasma Enhanced Chemical Vapor Deposition (PECVD) process to form a passivation layer of the sensor. This passivation layer can prevent direct exposure of the sensing elements to harsh media and enhance the reliability of the wind sensor. (h) After that, a 300 nm thick Au film was deposited and patterned on the other side of the sensor chip as the bonding pads. Figure 3a shows the enlarged photograph of the fabricated wind sensor. The overall dimension of the sensor chip is 4.6 mm × 4.6 mm × 0.18 mm, and the sensor consists of four heaters and nine thermistors. A central thermistor senses the average heater temperature, while the other eight, which are distributed symmetrically around the heaters, measure the temperature differences between the upstream and downstream surface of the sensor. Figure 3d shows the wind sensor was packaged in a protection shell, which protects them from the environment.

3 Modelling and simulation

3.1 Analytical model

For better understanding the working principle of the sensor and providing the guidelines to the design of the sensor, a simple one-dimensional analytical model of the thermal wind sensor and its package structure is established. Figure 4a shows the schematic layout of the sensor model, in which ①, ② and ③ respectively represents the fluid region, the sensor chip region and the package resin region. A heater of the length $2L_h$ lies in the middle of the sensor chip. Two temperature sensors are placed upstream and downstream the heater with a distance of L_0. When the fluid flows over the sensor, a momentum boundary layer and a thermal boundary layer will be established above the surface of the sensor chip. δ_x is the thickness of the momentum boundary layer, and $\delta_{t,x}$ is the thickness of the thermal boundary layer. In the model of the above described wind

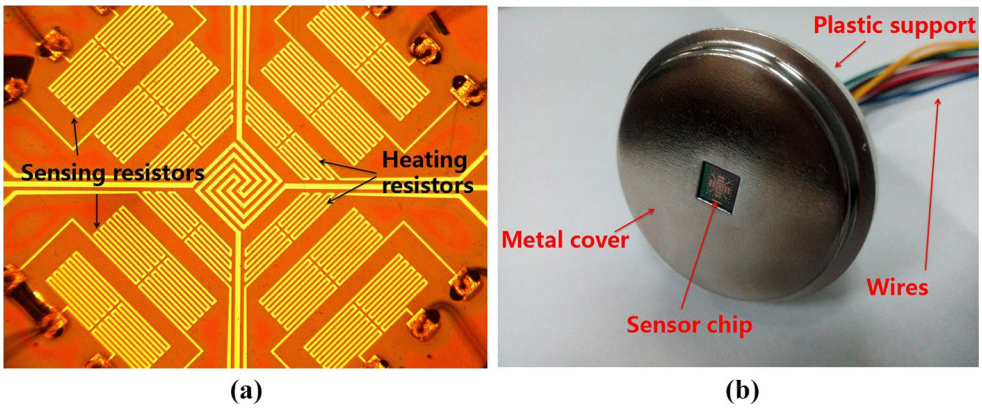

Fig. 3 The photograph of the fabricated wind sensor: **a** before packaging, **b** packaged in the protection shell

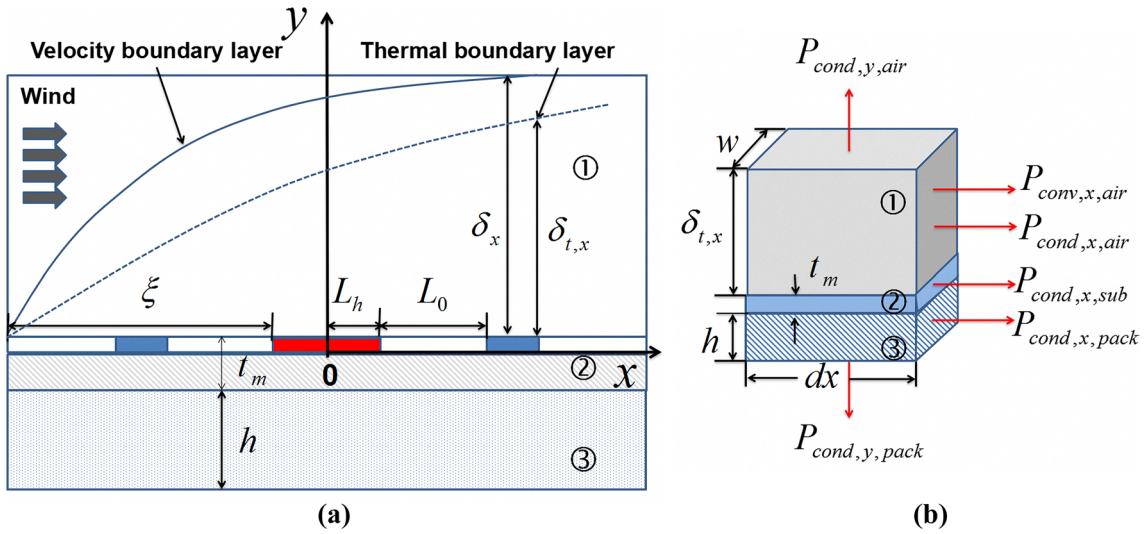

Fig. 4 **a** Schematic layout of the wind sensor model, **b** lumped element

sensor, we make the following assumptions (Lammerink et al. 1993; Nguyen and Dötzel 1997): (i) The heater generates a steady and constant heat power P_0 (DC condition); (ii) The magnitude T represents the over-temperature with respect to the ambient temperature T_∞ and flow in region ① is laminar and fully developed with average velocity U; (iii) The width of the chip is much larger than the thickness of the thermal boundary layer and the chip, i.e., $w \gg \delta_{t,x}$, t_m. Hence, the heat flow is considered to occur only in the xy-plane, i.e., the flow in the z-direction (out-of-plane in Fig. 4a) is neglected; and (iv) All structures in Fig. 4a have the same width w. These assumptions allow describing the system in terms of lumped elements. Figure 4b shows the lumped element of the model. As a result of the steady state, the total power entering the small section in Fig. 4b is zero, that is:

$$P_{cond,x,air} + P_{cond,x,sub} + P_{cond,x,pack} + P_{conv,air} + P_{cond,y,air} + P_{cond,y,pack} = 0. \quad (1)$$

Assuming that the flow velocity profile is linear within the momentum boundary layer and the temperature profile is linear within the thermal boundary layer and the package resin, then the following equations can be obtained based on Fourier's law:

$$P_{cond,x,air} = -k_{air} w \frac{\delta_{t,x}}{2} \frac{dT}{dx} \quad (2)$$

$$P_{cond,x,pack} = -k_{resin} w \frac{h}{2} \frac{dT}{dx} \quad (3)$$

$$P_{cond,x,sub} = -k_{sub} w t_m \frac{dT}{dx} \quad (4)$$

$$P_{cond,y,air} = \frac{k_{air} w T dx}{\delta_{t,x}} \tag{5}$$

$$P_{cond,y,pack} = \frac{k_{resin} w T dx}{h} \tag{6}$$

where k_{air}, k_{sub}, k_{resin} are respectively the thermal conductivity of the air, the sensor chip and the package resin. h and t_m are the thickness of the sensor chip and the package resin. T is the over-temperature with respect to the ambient temperature, and w is the width of the chip.

The power carried by convection can be expressed as:

$$\begin{aligned} P_{conv,x,air} &= \rho c_p w \int_0^{\delta_{t,x}} T_y U_y dy \\ &= \rho c_p w \int_0^{\delta_{t,x}} T \cdot \left(1 - \frac{y}{\delta_{t,x}}\right) \cdot U \cdot \frac{y}{\delta_x} dy \\ &= \rho c_p w T U \frac{\delta_{t,x}^2}{6\delta_x} \end{aligned} \tag{7}$$

where ρ and c_p are respectively the density and specific heat capacity of the air, U is the wind speed.

Combining Eqs. (1)–(7) and differentiating Eq. (1) yields the final differential equation:

$$6 k_{eq} t_{eq} \frac{d^2 T}{dx^2} - \rho c_p U \frac{\delta_{t,x}^2}{\delta_x} \frac{dT}{dx} - 6\left(\frac{k_{air}}{\delta_{t,x}} + \frac{k_{re}\sin}{h}\right) T = 0 \tag{8}$$

with

$$k_{eq} = \frac{k_{air}\frac{\delta_{t,x}}{2} + k_{re}\sin\frac{h}{2} + k_{sub} t_m}{t_{eq}} = \frac{k_{air}\frac{\delta_{t,x}}{2} + k_{re}\sin\frac{h}{2} + k_{sub} t_m}{\frac{\delta_{t,x}+h}{2} + t_m} \tag{9}$$

The magnitude k_{eq} represents the equivalent thermal conductivity in the x-direction while t_{eq} corresponds to the equivalent of the whole model. If the temperature of the heater is assumed to be homogeneous at T_0, after solving Eq. (8), the temperatures up- and downstream are:

$$T_u(x) = C_1 \exp(\lambda_1 x) + C_2 \exp(\lambda_2 x) \quad (x < -L_h) \tag{10}$$

$$T_d(x) = C_3 \exp(\lambda_1 x) + C_4 \exp(\lambda_2 x) \quad (x > L_h) \tag{11}$$

$$\lambda_{1,2} = \frac{\rho c_p \frac{\delta_{t,x}^2}{\delta_x}\left(U \pm \sqrt{U^2 + \frac{144 k_{eq} t_{eq} \cdot \delta_x^2}{(\rho c_p \delta_{t,x}^2)^2}\left(\frac{k_{air}}{\delta_{t,x}} + \frac{k_{re}\sin}{h}\right)}\right)}{12 k_{eq} t_{eq}} \tag{12}$$

The boundary conditions for Eqs. (10) and (11) is as follows:

$$T_u(-L_h) = T_0 = T_d(L_h) \tag{13}$$

$$T_u[-(L_h + \xi)] = T_d[L_h + \xi] = 0 \tag{14}$$

Where ξ is the distance from the edge of the heater to the border of the chip.

With the boundary conditions Eqs. (10) and (11) can be rewritten as follow:

$$T_u(x) = \frac{T_0\left[e^{\lambda_1 x} - e^{(\lambda_2-\lambda_1)(L_h+\xi)+\lambda_2 x}\right]}{e^{-\lambda_1 L_h} - e^{-\lambda_1(L_h+\xi)+\lambda_2 \xi}} \quad (x < -L_h) \tag{15}$$

$$T_d(x) = \frac{T_0\left[e^{\lambda_1 x} - e^{(\lambda_1-\lambda_2)(L_h+\xi)+\lambda_2 x}\right]}{e^{\lambda_1 L_h} - e^{(\lambda_1-\lambda_2)(L_h+\xi)+\lambda_2 L_h}} \quad (x > L_h) \tag{16}$$

Since two temperature sensors are located up- and downstream at a distance L_0 from the heater, the temperature difference between these two locations is given by:

$$\Delta T = T_d(L_0 + L_h) - T_u(-L_0 - L_h) \tag{17}$$

The heater temperature T_0 in Eqs. (15) and (16) can be determined by considering the total power entering and leaving the heater:

$$P_0 + P_{in,conv} = P_{out,cond} + P_{out,conv} \tag{18}$$

For small L_h, it can be assumed that $P_{in,conv} = P_{out,\,conv}$. Therefore, all the generated heat of the heater is dissipated mainly by diffusion, and Eqs. (18) can be rewritten as follow:

$$\begin{aligned} P_0 \approx P_{out,cond} = {} & \frac{2 k_{air} w L_h}{\delta_{t,x}} T_0 + \frac{2 k_{re}\sin w L_h}{h} T_0 \\ & + k_{eq} t_{eq} w\Big(C_3 \lambda_1 e^{-\lambda_1 L_h} + C_4 \lambda_2 e^{-\lambda_2 L_h} \\ & - C_1 \lambda_1 e^{\lambda_1 L_h} - C_2 \lambda_2 e^{\lambda_2 L_h}\Big) T_0 \end{aligned} \tag{19}$$

In this equation, the first and second terms of the right side account for the heat diffusion in y-direction, while the third term of the right side describes the heat diffusion in x-direction caused by the temperature gradient up- and downstream the heater. Therefore, the temperature of the heater can be expressed as:

$$T_0 = \frac{P_0}{\frac{2 k_{air} w L_h}{\delta_{t,x}} + \frac{2 k_{re}\sin w L_h}{h} + k_{eq} t_{eq} w\left(C_3 \lambda_1 e^{-\lambda_1 L_h} + C_4 \lambda_2 e^{-\lambda_2 L_h} - C_1 \lambda_1 e^{\lambda_1 L_h} - C_2 \lambda_2 e^{\lambda_2 L_h}\right)} \tag{20}$$

To ease the analytical solution of the above equation the parameters $\delta_{t,x}$ can be substituted by the average height of the thermal boundary layer,

$$\overline{\delta_{t,x}} = \frac{1}{2(L_h+\xi)} \int_{-L_h-\xi}^{L_h+\xi} \delta_{t,x}(x)dx \tag{21}$$

$$\frac{\delta_{t,x}}{\delta_x} = \frac{1}{1.026} \overline{\mathrm{Pr}}^{-1/3} = \frac{1}{1.026} \left(\frac{c_p \mu}{k_{air}}\right)^{-1/3} \tag{22}$$

$$\delta_x = 4.64(x + L_h + \xi)\left[\frac{\rho U(x+\xi+L_h)}{\mu}\right]^{-1/2} \tag{23}$$

Combining Eqs. (21)–(23), the average height of the thermal boundary layer could be calculated,

$$\overline{\delta_{t,x}} = \frac{1}{2(L_h+\xi)} \int_{-L_h-\xi}^{L_h+\xi} \delta_{t,x}dx = 4.269(L_h+\xi)^{1/2} U^{-1/2} \alpha^{1/3} \nu^{1/6} \tag{24}$$

where α is the thermal diffusivity of the air, and ν is the kinematic viscosity of the air.

Figure 5a shows how the temperature profile T(x) changes according to Eqs. (15), (16) and (20) as the flow velocity increases. The parameters used for these curves are summarized in Table 1. As expected, due to the increased convection, the heater temperature T_0 decreases with increasing velocity. Besides, upstream the temperature decay becomes steeper whereas downstream the temperature decay becomes flatter due to the forced convection. If the temperature sensors are located at a distance $L_0 = 0.6$ mm from the heater, the resulting ΔT is as shown in Fig. 5(b), which shows the typical response of a calorimetric flow sensor in constant power mode.

As shown in the above analytical model, the output temperature difference of the thermal wind sensor is related to some key structure parameters. Therefore, how these parameters affect the performance of the wind sensor are also investigated in this study. These investigations include six variables: the length of the heating element (L_h), the width of the heating element (w), the thickness of the chip and package resin (t_m and h), the size of the chip ($L_h + \xi$) and the distance between the heater and temperature sensors (L_0). When one parameter is varied, other parameters are kept constant. Results of thses investigations are shown in Fig. 6. From Fig. 6, some important conclusions can be drawn: (i) the sensitivity of the sensor will decrease with the size of the heating element, which means that the

Table 1 The structure parameters and material properties related to the sensor model

Parameters	Value
L_h	0.2 mm
L_0	0.6 mm
ξ	1.8 mm
w	4 mm
t_m	0.2 mm
h	3 mm
k_{air}	25.24e−3 W/(m K)
k_{sub}	1.13 W/(m K)
k_{resin}	0.48 W/(m K)
ρ	1.164 kg/m^3
c_p	1.013 kJ/(kg K)
ν	15.7e−6 m^2/s

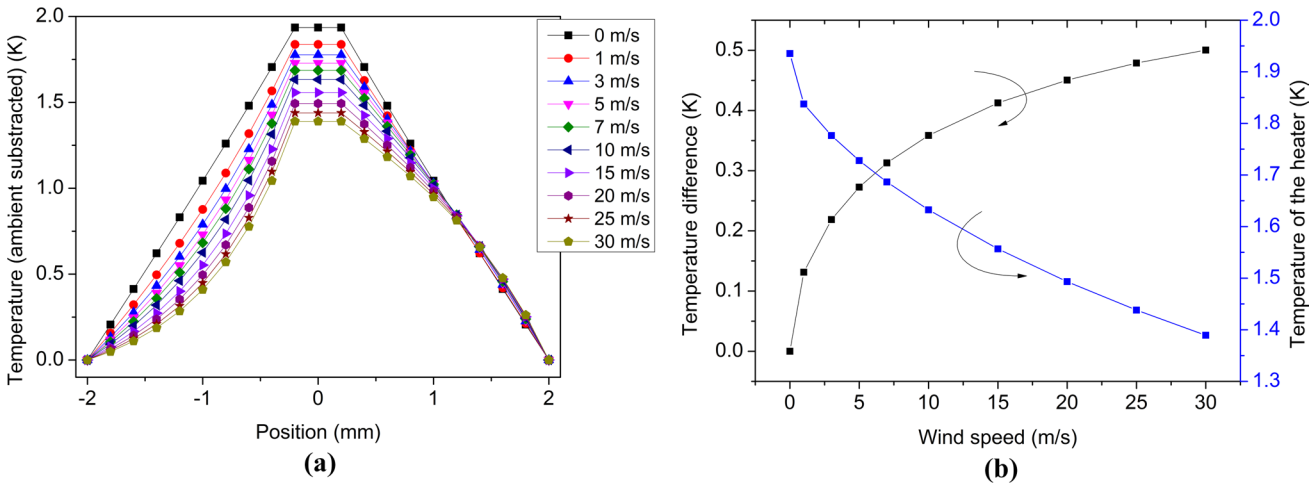

Fig. 5 **a** Analytical temperature profile at various speeds using the parameters summarized in Table 1, **b** analytical sensor output and the heater's temperature of the thermal wind sensor using the parameters summarized in Table 1

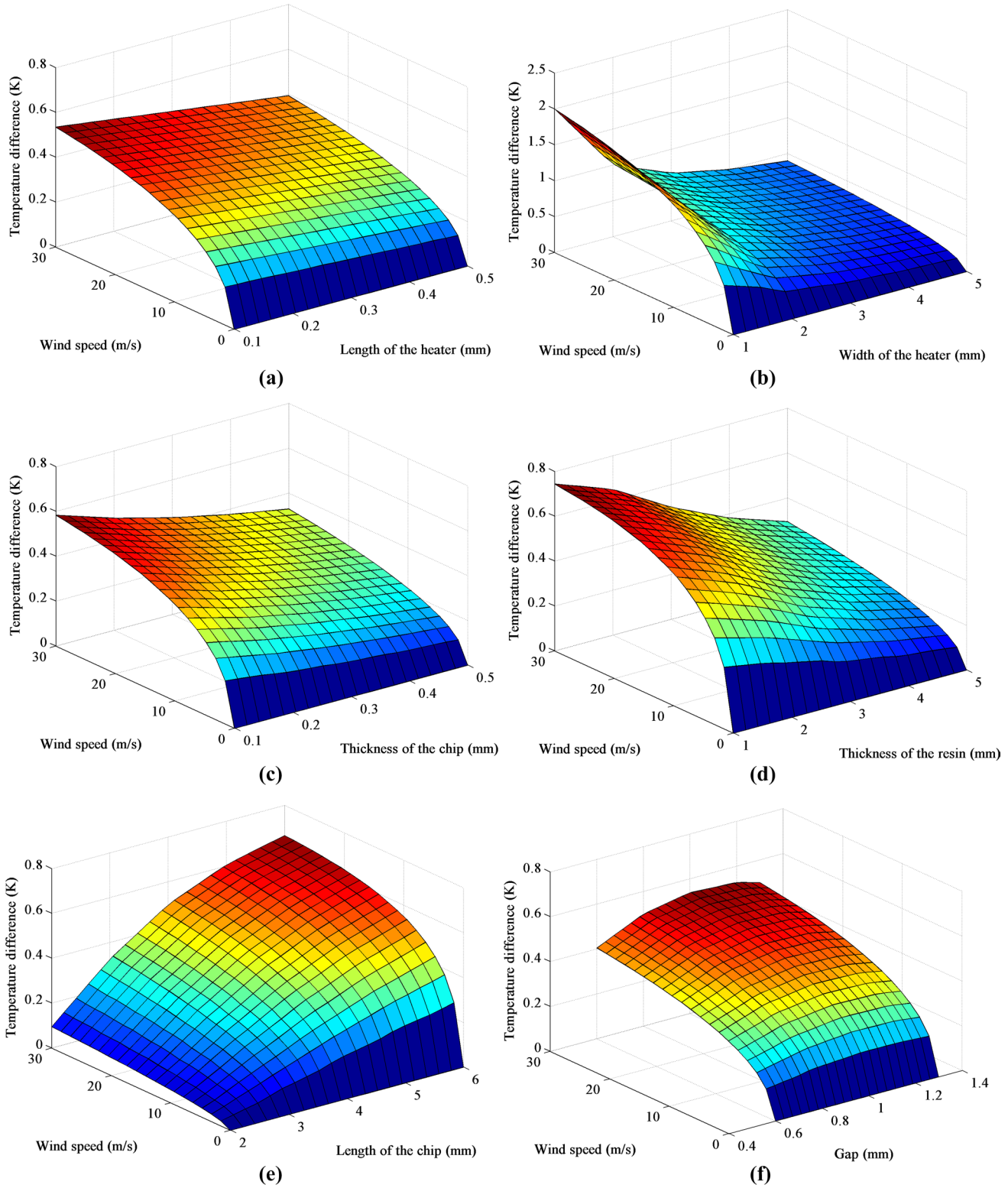

Fig. 6 Analytical results of the effect of structure parameters on the output temperature difference of the thermal wind sensor: **a** different lengths of the heating element (L_h), **b** different widths of the heating element (w), **c** different thicknesses of the chip (t_m), **d** different thicknesses of the package resin (**h**), **e** different sizes of the chip ($L_h + \xi$) and **f** different gaps between the heating element and temperature sensors (L_0)

smaller the heating element, the higher sensitivity can be obtained; (ii) the sensitivity of the sensor will decrease with the increase in the thickness of chip and package resin. This is because the thicker the chip and package resin are, the greater the heat loss generated in the horizontal direction; (iii) the sensitivity is directly proportion to the size of the chip. However, when chip size increases, the sensor cost will significantly increase. Thus the sensor should be optimized with the balance of price and performance; and (iv) the sensitivity of the sensor is not a monotonic function of the distance between the heater and temperature sensors, which means that in the design of the sensor an appropriate value should be chosen.

3.2 Finite element analysis

In order to verify the validity of the sensor model, a 2D FEM model of the thermal wind sensor including its package structure was built with COMSOL Multiphysics 4.2 software (Comsol Inc., 2016). The sensor model was composed of four parts, including a flow channel, a glass substrate, a metal heater and a package resin. The heaters were used to heat the substrate to a temperature above ambient, while the thermistors were omitted to shorten the solving time of the model. The dimensions and material properties of the model structures are shown in Table 1. The boundary conditions of the simulation model are as follows: the air, the chip and the encapsulation structure are defined respectively as the fluid and solid regions. The interface between the fluid and solid regions is defined as the coupling relationship. At the fluid inlet, the temperature was set to the room temperature (293 K) and the laminar inlet flow rate was set from 0 to 30 m/s. At the fluid outlet, the temperature boundary condition was set to outflow (convection dominated) and the fluid boundary condition was set to zero (relative) pressure. The initial temperature on the back surface of the sensor was the same as the room temperature. The sensor was operated at constant power (CP) mode and the heating power is set as 10 mW.

The simulation results are shown in Fig. 7. Comparing the simulation results shown in Fig. 7c with the theoretical results shown in Fig. 5b, it can be found that although the dimensions and material properties of the model are kept the same, the simulated heater's temperature is higher than the theoretical results and the output temperature difference of the sensor in the simulation is smaller than its theoretical results. This deviation is mainly caused by two factors: (1) in the analytical model the regional mean temperature T(x)/2 is used to make an approximate calculation of the lateral conductive heat transfer of the sensor. As a result, the conductive heat loss in the sensor is overestimated to a certain extent, causing the theoretical value of the heater's temperature is less than the simulation result; (2) In the analytical model the mean thickness of the thermal boundary layer over the entire chip surface is used to make an approximate calculation of the lateral convective heat transfer caused by the airflow, which makes the thermal convection effect on the upstream of the sensor surface is overestimated whereas the thermal convection effect on the downstream of the sensor surface is underestimated. Thus, when the wind speed increases, the temperature decrease on the upstream of the sensor surface is greater than the actual value, while the temperature decrease of the downstream is less than the actual value. This conclusion can also be verified by the comparison of the temperature distribution curve in Figs. 5a and 7b. Figure 7d shows the comparison between the normalized simulation results and calculated results with respect to the output temperature difference of the sensor. It can be seen from the figure, the two curves are in good agreement, indicating that despite a few drawbacks, the analytical model of the sensor can meet the need of theoretical analysis on the characteristics of the sensor in a certain range.

Based on the design rules concluded from the analytical model, the final design parameters of the sensor are determined as follows: the length of the heating element is 200 μm; the width of the heating element and the thickness of the chip are chosen as 650 and 180 μm, respectively. The distances between the sensing elements and the heaters were 270 and 540 μm. The size of the chip is 4.6 mm and the thickness of the package resin is 2 mm. The line width of the resistors was 15 μm, the same as the spacing between lines. The whole 3D sensor model is shown in Fig. 8. Figure 9a–d show the simulation results of the thermal profiles on the sensor surface when the wind speed is 10 m/s and the wind angles are respectively 0°, 30°, 60° and 90°. It can be observed that the temperature distribution on the sensor surface varies with the change of the wind direction. Besides, the temperature difference of the two orthogonal directions (T_{EW} and T_{NS}) all strictly follow the sine (cosine) curve, as shown in Fig. 9e. Figure 9f shows that the temperature difference signal between the upstream and downstream of the sensor surface changes with the wind speed when the wind angle is 0°. It can be seen from the figure that, with the increase of the wind speed, the chip's temperature decreases rapidly. Meanwhile, the temperature difference between the upstream and downstream of the sensor surface also increases with the increase of the wind speed. The internal temperature gradient of the chip reaches 1 K when the wind speed is 35 m/s.

4 Sensor characterization

4.1 DC characterization of the sensor

First, in order to measure the resistance of silicon vias, a test structure was designed. As shown in Fig. 10a, one side of

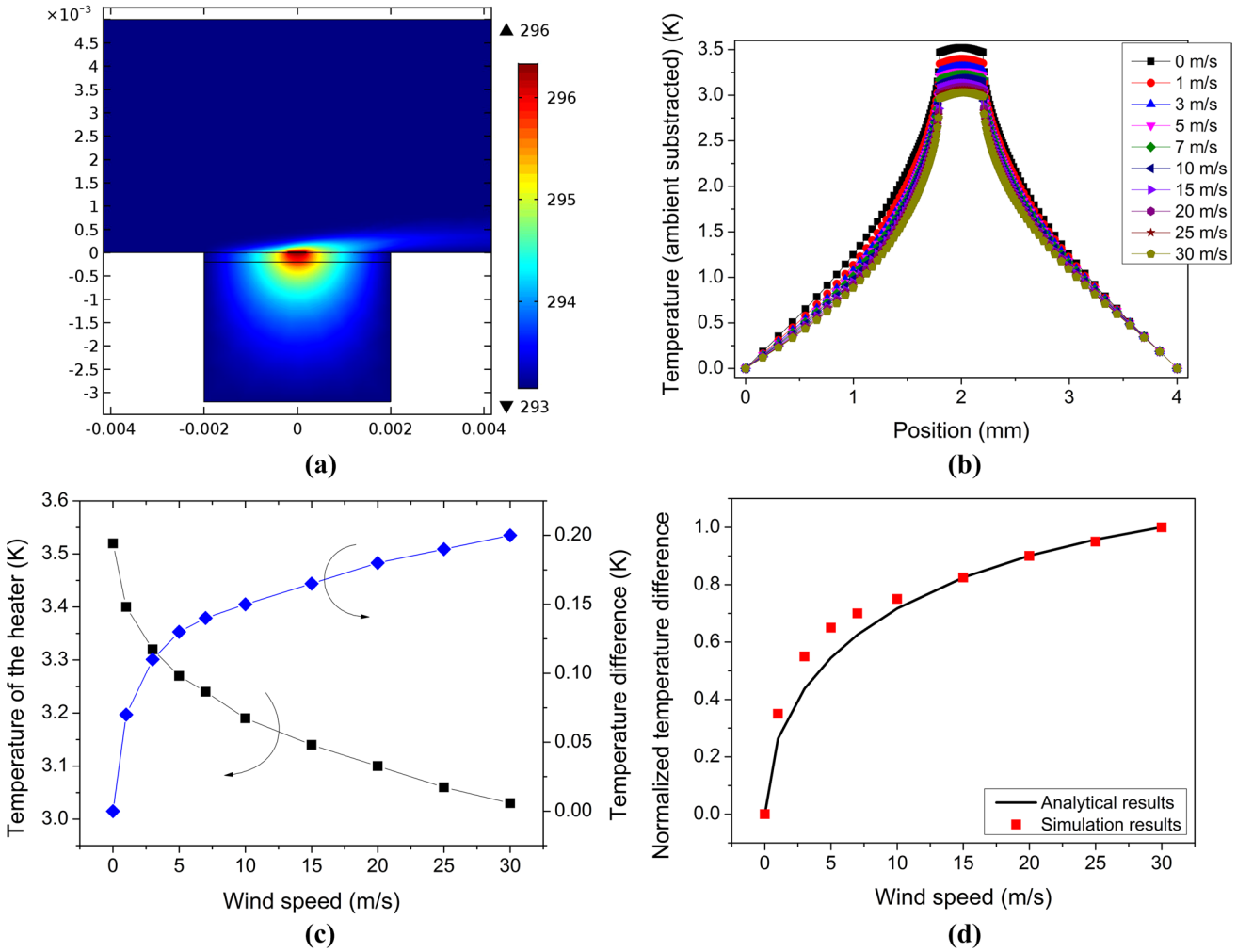

Fig. 7 Simulation results of the 2D sensor model: **a** the thermal profiles of the wind sensor with package resin, **b** the temperature distribution curve across the central axis of the sensor surface, **c** the output temperature difference and the heater's temperature of the sensor versus the wind speed, **d** comparison between simulation results and analytical results

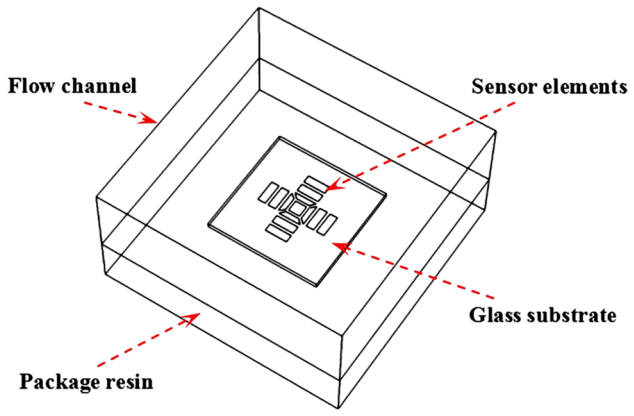

Fig. 8 The 3D model of the proposed thermal wind sensor, including the flow channel, the sensor chip and the package resin

silicon vias were connected by a Pt metal film, whose sheet resistance is 1.263 Ω per square and the total resistance is 11.8 Ω. Meanwhile, the other side of silicon vias were not connected and only covered by Au pads. A voltage-resistance characteristic curve of the test object can be obtained by applying a DC voltage to the two Au pads. During the measurement, two test samples were selected randomly. The applied voltage varies from 0 V to 1.5 V. Test results are shown in Fig. 10b. As can be seen from the figure, due to the negative temperature coefficient of the silicon material and Joule heating effect, the resistances of silicon vias decrease with the increase of the applied voltage. After deducting the Pt film resistance, the DC resistance of a single silicon vias is about 1.67–1.73 Ω (including the contact resistance between the silicon and the metal film).

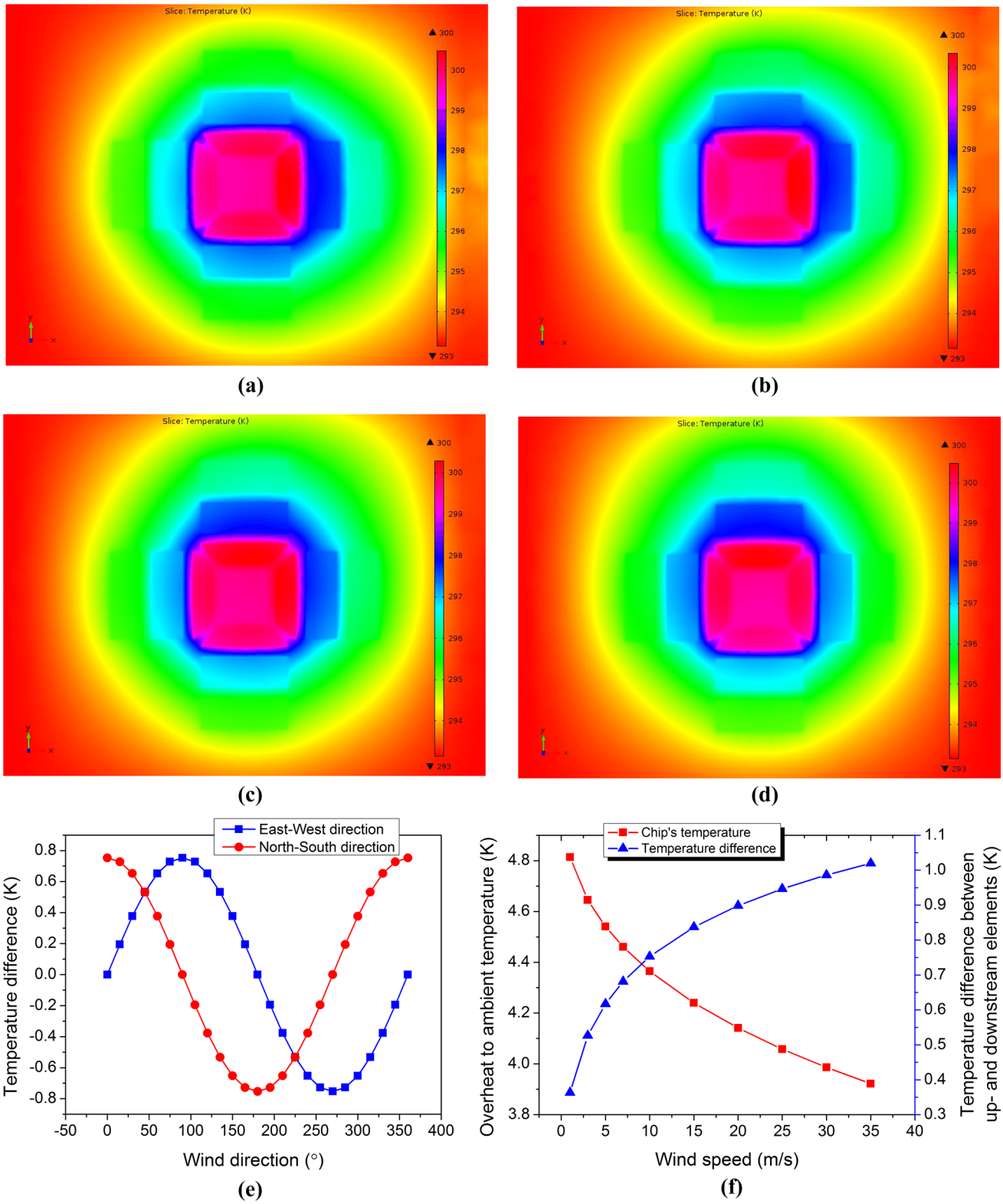

Fig. 9 Simualtion results of the 3D sensor model. The thermal profiles on the surface of the wind sensor versus different wind directions: **a** 0°, **b** 30°, **c** 60°, **d** 90°, **e** the temperature difference between the upstream and downstream sensor surface versus different wind directions when the wind speed is 10 m/s, **f** the temperature difference between the upstream and downstream sensor surface and the chip's central temperature versus different wind speeds when the wind direction is 0°

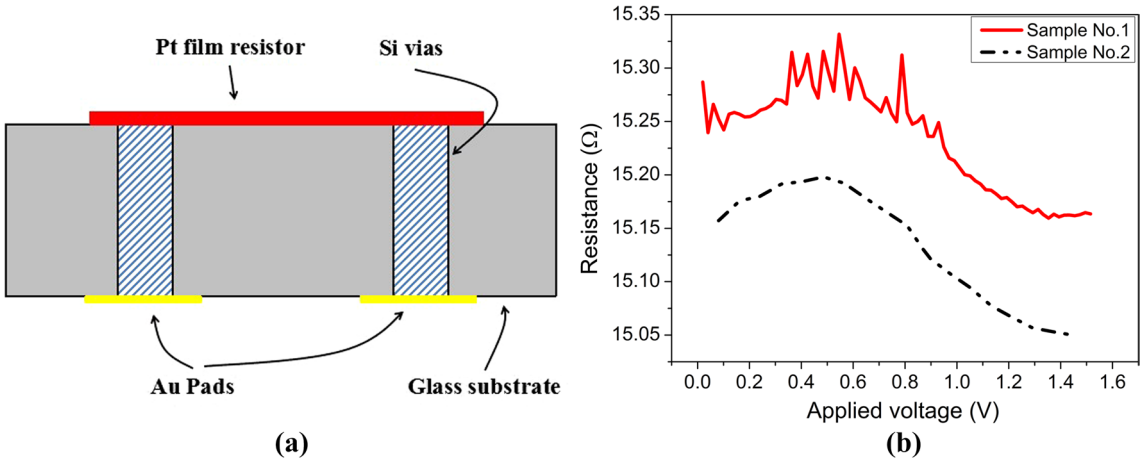

Fig. 10 **a** Schematic diagram of the test structure for measuring the resistance of the silicon vias. **b** The voltage–resistance characteristic curve of the test structure

Then, two-point probe measurement was used for investigating the electrical properties and thermal characteristics of the thin film Pt resistors at zero flow rate and ambient atmospheric conditions. The resistance of the fabricated heaters and sensing thermistors were 500 and 830 Ω at room temperature, respectively. To obtain the TCR of the sputtered Pt thermistor, the wind sensor was first put into a sealed plastic box, then the sealed box was put into a temperature chamber which can offer a steady temperature condition from 233 to 423 K with ±0.3 K fluctuation to 373 K. The resistance output of the thermistor was recorded when the temperature changed from 273 to 323 K. The results are shown in Fig. 11a. As can be seen from the figure, the output of the sensor has a linear relationship with the changes of the temperature. After calculation, the TCR value of the Pt thin film is found to be 1778 ppm/K.

Finally, a Keithley 2400 source meter was utilized to gradually increase the applied voltage to the heater and measure the resistance of the heater and the current flowing through the heater simultaneously. By using TCR measured previously, the temperature of the heater can be obtained from the corresponding resistance of the heater. Figure 11b shows the temperature of the heater was plotted versus the corresponding heating voltage on the heater. As can be observed from the figure, the temperature of the heater has a quadratic relationship with the heating voltage. This result can be attributed to the fact that the Joule heat generated from the Pt heater is essentially proportional to the square of the heating voltage.

4.2 Output characteristics of the sensor

As shown in Fig. 12, the complete sensor was mounted onto the top surface of a circular sample holder, which was inserted into a rectangular wind tunnel and exposed with the sensor surface to the flow. The wind speed of the

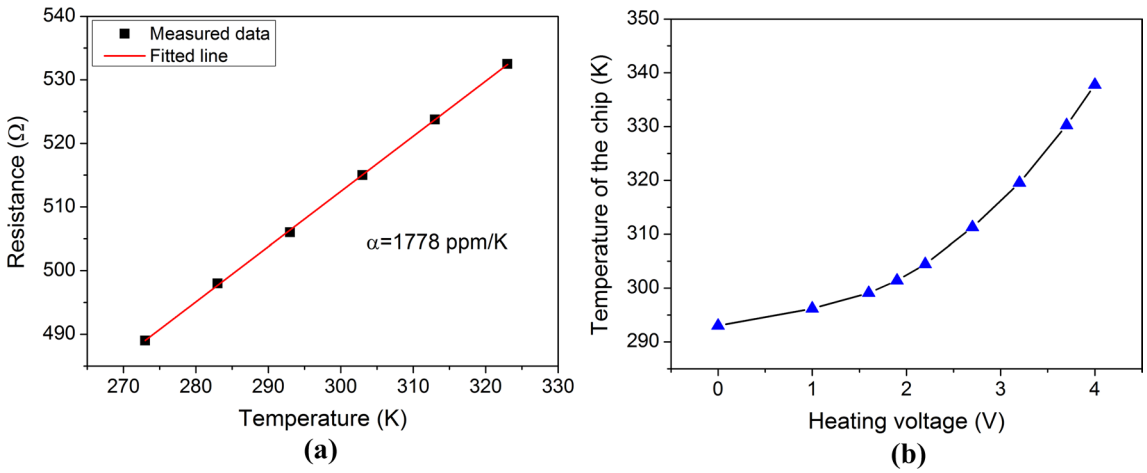

Fig. 11 **a** Resistance vs. temperature relationship of the Pt heater. **b** The dependence of the heater temperature on applied heating voltage

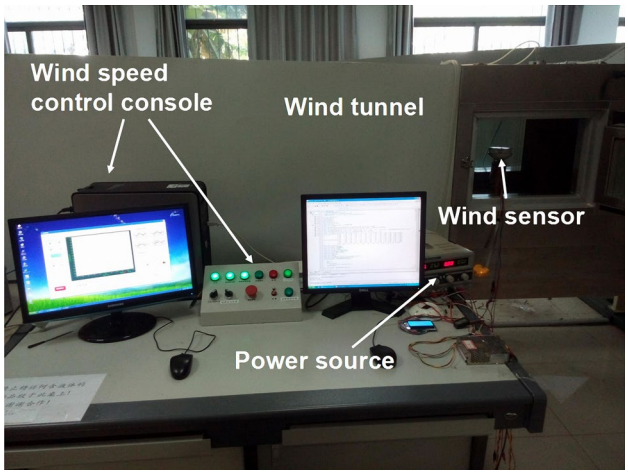

Fig. 12 The photograph of the wind tunnel test equipment and the thermal wind sensor tested in the channel

wind tunnel ranged from 0 to 30 m/s, with a resolution of 0.2 m/s. The direction sensitivity of the sensor was measured by rotating the sample holder with the sensor around its axis under a constant flow velocity in the tunnel. The temperature of the airflow in the tunnel can be regulated by the cooling and heating system. By using this set-up, the operating temperature can be adjusted with ±0.5 °C accuracy. In the measurement, a low-offset instrument amplifier AD623 with 300 times amplification first boosted the output voltage of the sensor. Thereafter, the analog signals were digitized by a 10-bit ADC of the C8051F410 microprocessor. Finally, the data was displayed on a liquid crystal display (LCD). The readout electronics circuit was implemented on a printed circuit board (PCB) and had a power consumption of 153 mW.

In order to know the sensitivity and measurement range of the proposed MEMS thermal wind sensor, the output voltages of the sensor in two directions were recorded and plotted versus different wind speeds and wind directions in Fig. 13a, b. In the experiment, the ambient temperature was about 300 K and the heating powers applied on the heaters and the thermistors were respectively 11.5 and 3 mW. As shown in Fig. 13c, close agreements can be observed between the output voltages of the sensor in

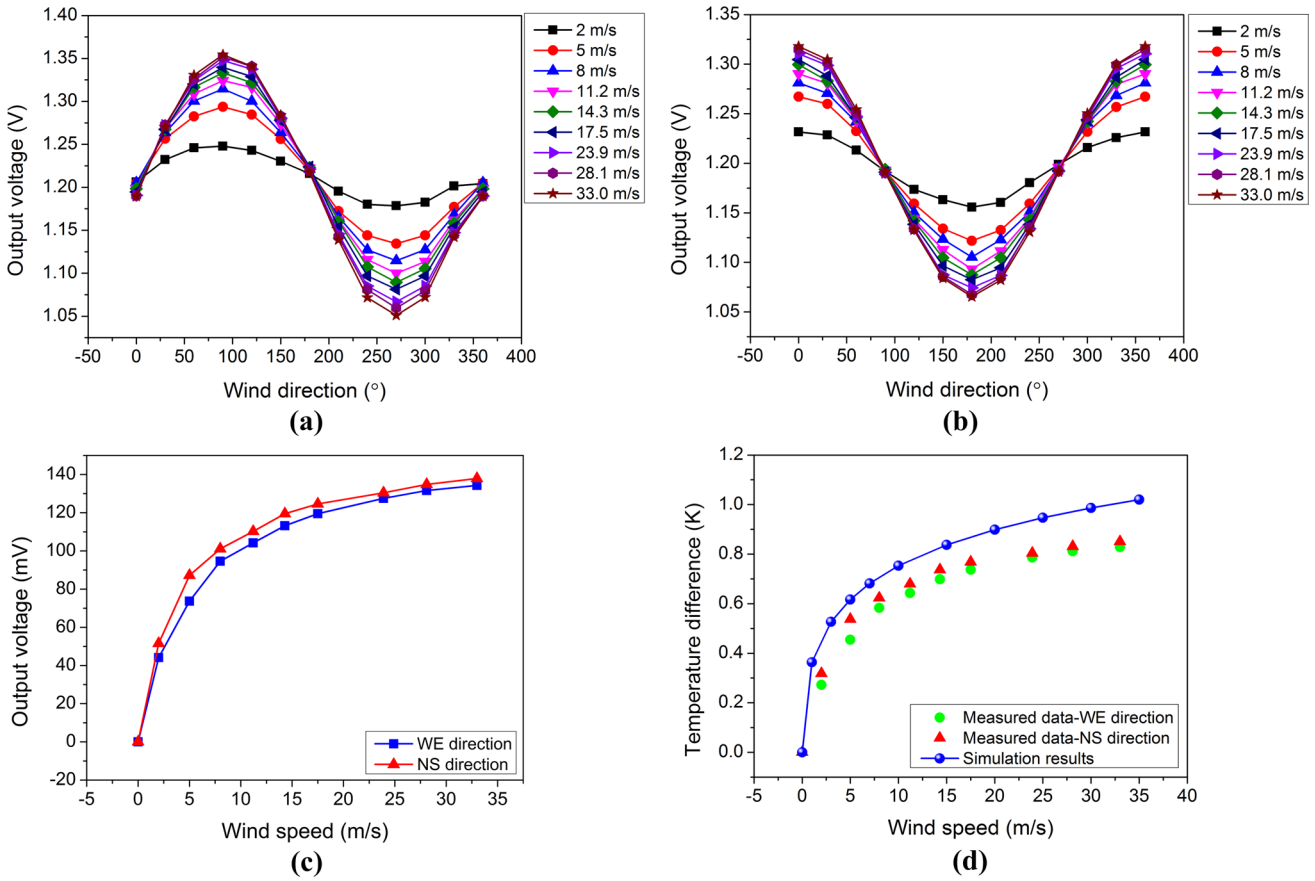

Fig. 13 The sensor's outputs in two channels under the condition of different wind speeds and wind directions: **a** output voltages in East–West direction, **b** output voltages in North–South direction, **c** comparison of output voltages in two directions, and **d** comparison of measurement results and simulation results

two channels, which shows that the structural symmetry of the sensor is good. Measurement results also show that when the total heating powers of the sensor were 14.5 mW, the sensor can measure the wind speed up to 33 m/s and the measured sensitivity at 5 m/s is 20.2 mV/(m/s) after 300 times amplification. Figure 13d shows the simulated and measured output temperature differences of the sensor versus wind speeds. As can be seen, the measured results are slightly smaller compared to the simulation results. Meantime, the measured sensitivities present a quicker descending trends than the simulation. The most important reason accounts for this phenomenon is that in the simulation the sensor model was simplified and in the experiment there were still some conductive heat losses caused by the conducting paths such as thin-film gold leads and metal protective shell.

With the calibrated model (Zhu et al. 2015) and the measured data the accuracy of the proposed thermal wind sensor can be determined. The wind sensor was exposed to wind speeds of 2, 5, 8, 12.7, 17.5 and 23.9 m/s from 12 equally spaced angles. Figure 14 shows the error plots for the sensor for six wind speeds from 12 angles. Each line of the plots shows the error of the sensor at one wind speed. The left graph shows the absolute speed error of the sensor; the error is smaller than 0.5 m/s in the range of 0–15 m/s, and for other wind speeds the error is smaller than 5% of the full-scale (FS). The loss of accuracy at high wind speeds is attributed to a loss in the sensitivity of the sensor with the increase of the wind speed. The right graph shows the wind angle measurement error of the sensor. The error is smaller than 5° in all cases.

The sensor repeatability refers to the successive runs made by using a single sensor to evaluate discrepancies in its response (Gao et al. 2005). The repeatability of the sensor was studied in this work by using the same sensor to repeatedly measure the wind speed and direction at different times. The time interval is 15 days. Figure 15 shows the measured output wind speed and direction for different measurement conditions. As can be observed, the sensor's output results have close agreements among different measurements, which indicate that the proposed thermal wind sensor has a good repeatability.

Table 2 summarizes performances of 2D MEMS thermal wind sensors recently reported which are operated in constant power mode. Thanks to the Glass-in-Silicon substrate, the reliability of electrical connection of the thermal wind sensor mentioned in this work is excellent, while the reliability of sensor structure is also good. At the same time, because the sensing elements are thermally isolated from the heaters, small power consumption were needed in the measurement, and the measurement range were wided directly by selecting the appropriate distance between the heaters and the sensing elements. A performance measurement for the micromachined wind sensor was performed and the tested results showed that the sensor had a good measurement accuracy and was still well after the cycle-testing.

5 Conclusions

In this paper, we modeled and characterized a robust, low-power and wide-range MEMS thermal wind sensor. The sensor was fabricated by the glass reflow process and operated in the calorimetric principle. The calculated results derived from the analytical model have shown that the structure parameters such as chip dimension and thickness, heater length and width, and the distance between the heater and the sensing elements, have an important effect on the sensor performance. The little

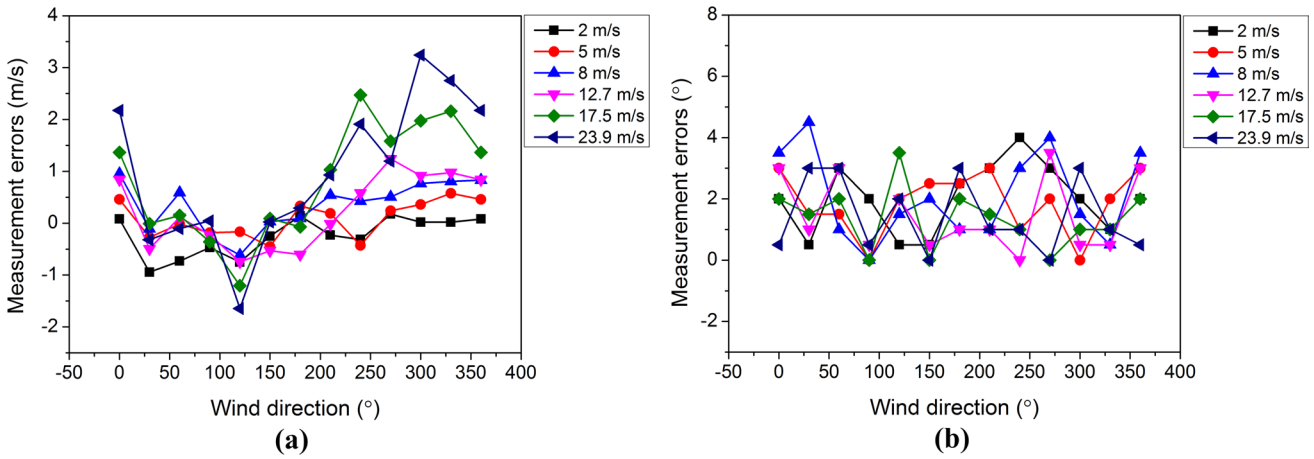

Fig. 14 Measured **a** wind speed errors and **b** wind direction errors of the proposed thermal wind sensor under the condition of different wind speeds and wind directions

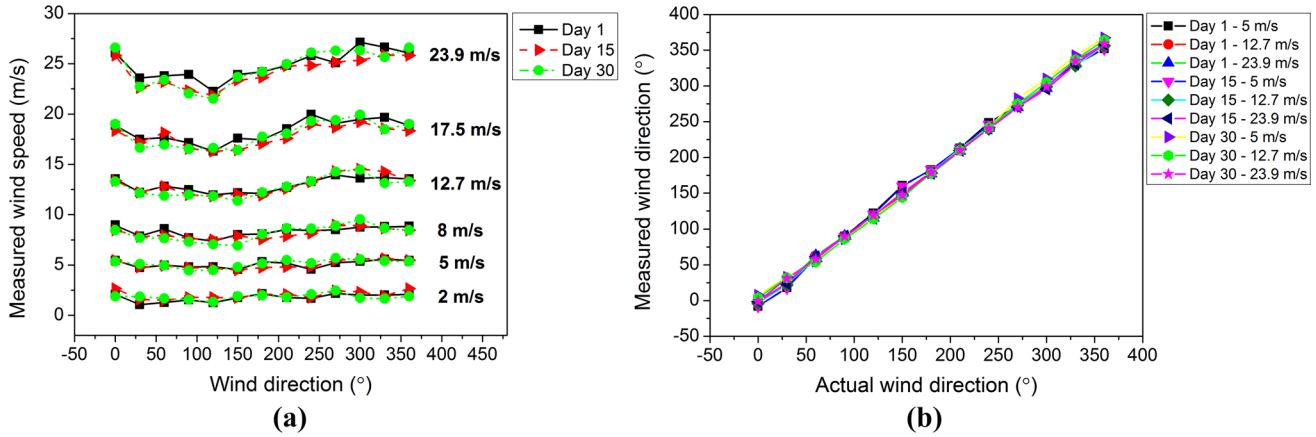

Fig. 15 The repeatability of the proposed thermal wind sensor: **a** wind speed measurement and **b** wind direction measurement under the condition of different wind speeds and wind directions

Table 2 Performance comparison of different 2D MEMS thermal wind sensors

References	Cubukcu et al. (2010)	Bruschi et al. (2009)	Kim et al. (2003)	Adamec et al. (2010)	Dominguez et al. (2008)	Shen et al. (2010)	Zhu et al. (2016)	This work
Measurement speed range (m/s)	0–5	0.9–8.4	0–10	0–20	0–20	0–10	0–17.5	0–33
Measurement angle range (°)	0–360	0–360	0–360	0–360	0–360	0–360	0–360	0–360
Power dissipation (mW)	0.5	4	300	50	52.8	100	4.8–43.3	14.5
Accuracy of wind speed measurement (m/s)								
Low speeds	0.01	±1% FS	Not given	±2% FS	0.3	0.5	Not given	<0.5
High speeds								<5% FS
Accuracy of wind angle measurement (°)	3.5	8	5	Not given	10	5	<6	<5
Substrate structure	SiO_2/Si_3N_4 membrane	Si_3N_4 membrane	Silicon membrane	Si_3N_4 membrane	Silicon substrate	Glass substrate	Glass-in-silicon substrate	Glass-in-silicon substrate
Reliability of electrical connection	Low	Low	Low	Low	Low	Low	High	High
Reliability of sensor structure	Low	Low	Low	Low	High	High	High	High

difference between the simulation and theoretical reduction results validated the rightness and feasibility of the theory. From the COMSOL simulation and the experiment data, we can see that the sensor can achieve a wide measurement range with a low power consumption. The total heating power consumption of the sensor was only 14.5 mW and the wind speeds were measured up to 33 m/s with an accuracy better than 0.5 m/s at low speed ranges and 5% FS at high speed ranges. Wind directions over the full range of 360° were measured with an accuracy of 5°.

Acknowledgements The project is supported partly by the High-Tech Research and Development of China under Grant 2013AA041106 and partly by the Innovation Project for Graduate Student of Jiangsu Province under Grant KYLX15_0099.

References

Adamec RJ, Thiel DV (2010) Self heated thermo-resistive element hot wire anemometer. IEEE Sens J 10(4):847–848

Arritt RW, Clark CA, Goggi AS, Sanchez HL, Westgate ME, Riese JM (2007) Lagrangian numerical simulations of canopy air flow effects on maize pollen dispersal. Field Crops Res 102(2):151–162

Aylor DE (1990) The role of intermittent wind in the dispersal of fungal pathogens. Annu Rev Phytopathol 28:73–92

Baltes H, Paul O, Brand O (1998) Micromachined thermally based CMOS microsensors. Proc IEEE 86(8):1660–1678

Bruschi P, Dei M, Piotto M (2009) A low-power 2-D wind sensor based on integrated flow meters. IEEE Sens J 9(12):1688–1696

Chen J, Liu C (2003) Development and characterization of surface micromachined out-of-plane hot-wire anemometer. J Microelectromech Sys 12(6):979–988

Comsol (2016) FEA Commercial Software, Burlington, 1997–2016. http://www.comsol.com

Connell JR (1982) The spectrum of wind speed fluctuations encountered by a rotating blade of a wind energy conversion system. Sol Energy 29(5):363–375

Cubukcu AS, Zernickel E, Buerklin U, Urban GA (2010) A 2D thermal flow sensor with sub-mW power consumption. Sens Actuators A 163(2):449–456

Dominguez M, Jiménez V, Ricart J, Kowalski L, Torres J, Navarro S, Castañer L (2008) A hot film anemometer for the Martian atmosphere. Planet Space Sci 56(8):1169–1179

Ebefors T, Kälvesten E, Stemme G (1998) Three dimensional silicon triple-hot-wire anemometer based on polyimide joints. In: Proceedings of IEEE. Eleventh annual international workshop on micro electro mechanical systems. An investigation of micro structures, Heidelberg, pp 93–98

Gao F, Wang L, Tang L, Zhu C (2005) A novel nano-sensor based on rhodamine-β—isothiocyanate-doped silica nanoparticle for pH measurement. Microchim Acta 152(1–2):131–135

Harman GG (1993) Reliability and yield problems of wire bonding in microelectronics. International Society for Hybrid Microelectronics, New York

Kaltsas G, Nassiopoulos A, Nassiopoulou AG (2002) Characterization of a silicon thermal gas-flow sensor with porous silicon thermal isolation. IEEE Sens J 2(5):463–475

Kim S, Kim S, Kim Y, Park S (2003) A circular-type thermal flow direction sensor free from temperature compensation. Sens Actuators A 108(1):64–68

Kumar P, Fennell P, Britter R (2008) Effect of wind direction and speed on the dispersion of nucleation and accumulation mode particles in an urban street canyon. Sci Total Environ 402(1):82–94

Lammerink TS, Tas NR, Elwenspoek M, Fluitman JH (1993) Micro-liquid flow sensor. Sens Actuators A 37:45–50

Li YB, Jiang ZB (2008) An overview of reliability and failure mode analysis of microelectro-mechanical systems (MEMS). Handbook of Performability Engineering, London, pp 953–966

Liu S, Pan S, Xue F, Nay L, Miao JM, Norford LK (2015) Optimization of hot-wire airflow sensors on an out-of-plane glass bubble for 2-D detection. J Microelectromech Syst 24(4):940–948

Nguyen NT (1997) Micromachined flow sensors—a review. Flow Meas Instrum 8(1):7–16

Nguyen NT, Dötzel W (1997) Asymmetrical locations of heaters and sensors relative to each other using heater arrays: a novel method for designing multi-range electrocaloric mass-flow sensors. Sens Actuators A 62(1):506–512

Sabaté N, Santander J, Fonseca L, Gràcia I, Cané C (2004) Multi-range silicon micromachined flow sensor. Sens Actuators A 110(1):282–288

Sadeghi MM, Peterson RL, Najafi K (2013) Air flow sensing using micro-wire-bonded hair-like hot-wire anemometry. J Micromech Microeng 23:085017

Shen GP, Qin M, Huang QA (2010) A cross-type thermal wind sensor with self-testing function. IEEE Sens J 10(2):340–346

Vilares R, Hunter C, Ugarte I, Aranburu I, Berganzo J, Elizalde J, Fernandez LJ (2010) Fabrication and testing of a SU-8 thermal flow sensor. Sens Actuators B 147(2):411–417

Zhao R, Sun S, Ding R (2004) Conditioning strategies of indoor thermal environment in warm climates. Energy Build 36(12):1281–1286

Zhu YQ, Chen B, Qin M, Huang QA (2014) 2-D micromachined thermal wind sensors—a review. IEEE Internet Things J 1(3):216–232

Zhu YQ, Chen B, Qin M, Huang JQ, Huang QA (2015) Development of a self-packaged 2D MEMS thermal wind sensor for low power applications. J Micromech Microeng 25(8):085011

Zhu YQ, Chen B, Gao D, Qin M, Huang QA, Huang JQ (2016) A robust and low-power 2-D thermal wind sensor based on a glass-in-silicon reflow process. Microsyst Technol 22(1):151–162